

APPLICATION OF THE SWE-TO-PWE ANTENNA DIAGNOSTICS TECHNIQUE TO AN OFFSET REFLECTOR ANTENNA

Cecilia Cappellin^{1,2}, Aksel Frandsen¹, Olav Breinbjerg²

¹ TICRA, Læderstræde 34, DK-1201 Copenhagen K, Denmark

² Ørsted•DTU, Technical University of Denmark, DK-2800 Kgs. Lyngby, Denmark

ABSTRACT

A new antenna diagnostics technique has been developed for the DTU-ESA Spherical Near-Field Antenna Test Facility at the Technical University of Denmark. The technique is based on the transformation of the Spherical Wave Expansion (SWE) of the radiated field, obtained from a spherical near-field measurement, to the Plane Wave Expansion (PWE), and it allows an accurate reconstruction of the field in the extreme near-field region of the antenna under test (AUT), including the aperture field. While the fundamental properties of the SWE-to-PWE transformation, as well as the influence of finite measurement accuracy, have been reported previously, we validate here the new antenna diagnostics technique through an experimental investigation of a commercially available offset reflector antenna, where a tilt of the feed and surface distortions are intentionally introduced. The effects of these errors will be detected in the antenna far-field pattern, and the accuracy and ability of the diagnostics technique to subsequently identify them will be investigated. Real measurement data will be employed for each test case.

Keywords: Antenna diagnostics, spherical near-field measurements, spherical wave expansion, plane wave expansion, offset reflector antenna.

1. Introduction

Electrical and mechanical errors in an antenna may seriously affect the antenna's performance. Though their presence is usually observed by anomalies in the antenna's far-field pattern, their identification is normally possible only through an analysis of the antenna's extreme near-field. The reconstruction of the extreme near-field on the basis of near- or far-field measurements is thus an essential step in antenna diagnostics.

Several non-invasive diagnostics techniques have been proposed over the years [1]-[3]: [1] computes the aperture field from planar near-field measurements, [2] studies and detects the errors caused by radome defects on basis of spherical near-field measurements while [3] reconstructs

the induced currents on the surface of big reflectors starting from far-field data.

When the field is expressed as a SWE obtained from a spherical near-field measurement, as is the case at the DTU-ESA Spherical Near-Field Antenna Test Facility [4], the calculation of the extreme near-field is anyway not straightforward since the SWE is valid only outside the antenna minimum sphere of radius r_o , see Fig. 1.

One way to circumvent this limitation is to transform the SWE into the PWE, which is valid on any z -plane $z > z_o$, with z_o being the largest z -coordinate of the source; note that $|z_o| \leq r_o$, see Fig. 1. Once the PWE is known, the extreme near-field can be computed by an inverse Fourier transform (IFT) and then subjected to diagnostics. This constitutes the basis of the recently developed SWE-to-PWE antenna diagnostics technique [5]-[6]. The technique uses spherical near-field measurement data to compute the field on a plane located in the extreme near-field of the AUT, and provides a spatial resolution that may, in principle, exceed the traditional limit of half a wavelength.

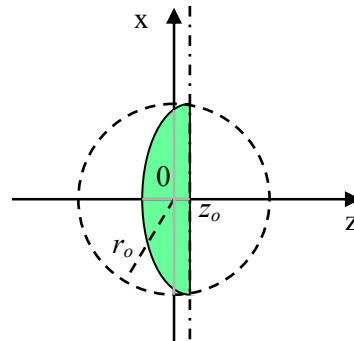


Figure 1. Spatial domains of validity of the SWE and PWE for a general antenna: the PWE is valid for $z > z_o$, the SWE for $r > r_o$.

The purpose of this work is to perform an experimental validation of the SWE-to-PWE antenna diagnostics technique under typical measurement conditions. To this end, we employ a cheap and simple commercially available offset reflector antenna for satellite TV reception, which in its nominal configuration already exhibits several non-ideal characteristics. We then introduce three additional errors, viz. a tilt of the feed, a

localized bump in the reflector, and a global distortion of the reflector surface. The near-fields are measured on a spherical surface, and transformed to the corresponding far-fields, where the effects of the errors are observed. The extreme near-field is then computed with the new antenna diagnostics technique with the purpose of identifying those errors.

The paper is organized as follows: In Section 2 the SWE-to-PWE diagnostics technique and its properties are briefly summarized, in Section 3 the offset reflector antenna is described, while the errors and the diagnostics results are presented in Section 4. All quantities are expressed in the S.I. rationalized system with the $e^{-i\omega t}$ time convention.

2. The SWE-to-PWE antenna diagnostics technique

We start by introducing the SWE of the electric field \bar{E} radiated by an antenna circumscribed by a minimum sphere of radius r_o , [7],

$$\bar{E}(\bar{r}) = \frac{k}{\sqrt{\eta}} \sum_{n=1}^{\infty} \sum_{m=-n}^n Q_{1mn}^{(3)} \bar{F}_{1mn}^{(3)}(\bar{r}) + Q_{2mn}^{(3)} \bar{F}_{2mn}^{(3)}(\bar{r}), \quad r > r_o \quad (1)$$

where $Q_{1mn}^{(3)}$ and $Q_{2mn}^{(3)}$ are the expansion coefficients and $\bar{F}_{1mn}^{(3)}(\bar{r})$ and $\bar{F}_{2mn}^{(3)}(\bar{r})$ are the power-normalized spherical vector wave functions. The medium intrinsic admittance is η , k is the wave number, and \bar{r} is the position vector expressed in terms of spherical coordinates (r, θ, φ) or rectangular coordinates (x, y, z) . In practice, the n -summation of the SWE is typically truncated at $N = kr_o + 10$ since this is sufficient for an accurate calculation of the far-field. The PWE of the same electric field \bar{E} in the spectral $k_x k_y$ -domain valid for $z > z_o$ is given by [8],

$$\bar{E}(x, y, z) = \frac{1}{2\pi} \int_{-\infty}^{\infty} \int_{-\infty}^{\infty} \bar{T}(k_x, k_y, z) e^{ik_z z} e^{i(k_x x + k_y y)} dk_x dk_y \quad (2)$$

where k_x and k_y are the spectral variables and $k_z = \sqrt{k^2 - k_x^2 - k_y^2}$. The plane wave spectrum for a given z -coordinate is $\bar{T}(k_x, k_y, z) \equiv \bar{T}(k_x, k_y) e^{ik_z z}$. The spectral domain is divided into two regions, the visible region, for $k_x^2 + k_y^2 \leq k^2$, which contains the propagating plane waves, and the invisible region, for $k_x^2 + k_y^2 > k^2$, which contains the evanescent plane waves, see Fig. 2. The two variables k_x and k_y are real, while k_z is real in the visible region but purely imaginary with a positive imaginary part in the invisible region. In practice, the k_x - and k_y -integrals are truncated at finite values $\pm k_{xmax}$ and $\pm k_{ymax}$ respectively, providing a spatial resolution (δ_x, δ_y) in the

aperture field equal to $\delta_x = \pi / k_{xmax}$, $\delta_y = \pi / k_{ymax}$. At the border between the visible and invisible regions $k_z = 0$ and the PWE generally possesses a singularity there [8].

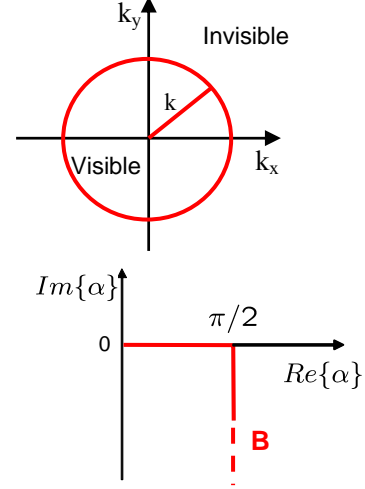


Figure 2. Visible and invisible regions of the spectral $k_x k_y$ -domain, and B contour of the variable α .

It can be shown [5]-[6] that the SWE of Eq. 1 can be rigorously transformed into the PWE of Eq. 2, allowing the plane wave spectrum $\bar{T}(k_x, k_y, z)$ to be written as

$$\bar{T}(k_x, k_y, z) = \sum_{n=1}^{\infty} \sum_{m=-n}^n Q_{1mn}^{(3)} \bar{T}_{1mn}(k_x, k_y, z) + Q_{2mn}^{(3)} \bar{T}_{2mn}(k_x, k_y, z) \quad (3)$$

where

$$\bar{T}_{1mn}(k_x, k_y, z) = \frac{e^{ik_z z}}{k_z} \frac{(-i)^{n+1}}{\sqrt{\eta} \sqrt{n(n+1)}} \bar{Y}_n^m(\alpha, \beta) \quad (4)$$

$$\bar{T}_{2mn}(k_x, k_y, z) = \frac{e^{ik_z z}}{k_z} \frac{(-i)^n}{\sqrt{\eta} \sqrt{n(n+1)}} \hat{k} \times \bar{Y}_n^m(\alpha, \beta) \quad (5)$$

with $\hat{k} = \bar{k} / k = (k_x \hat{x} + k_y \hat{y} + k_z \hat{z}) / k$. The function $\bar{Y}_n^m(\alpha, \beta)$ is the vector spherical harmonics [5], $\alpha \in B$, see Fig. 2, and is equal to $\alpha = \text{acos}(k_z / k)$, while $\beta \in [-\pi, \pi]$ and is equal to $\beta = \text{atan}(k_y / k_x)$. Eq. 3 shows that the plane wave spectrum on any z -plane $z > z_o$ can be expressed as a series of the same type and with the same Q coefficients of the SWE of Eq. 1, where the only difference lies in the basis functions that are now the vector spherical harmonics instead of the power-normalized spherical vector wave functions. The imaginary values of the angle α correspond to the

invisible region of the k_x, k_y -domain. Though the functions $\bar{Y}_n^m(\alpha, \beta)$ have an exponential growth in that region, it is important to note that the series of Eq. 3 is convergent in the entire spectral domain. Nevertheless, while the visible region of the spectrum reaches convergence with $N \approx kr_o$ terms, the invisible requires many more terms to compensate the exponential growth of the spherical harmonics [5]-[6]. In practice the finite dynamic range of the measurement system limits the measurement of these high order modes. However, it has been shown [6] that the recovery of the visible region and the singularity for $k_z = 0$, both correctly represented by the first $N \approx kr_o$ modes, provides accurate aperture fields that facilitate an effective diagnostics.

3. The offset reflector antenna: model and nominal configuration

The AUT is a 12GHz offset parabolic reflector, defined in the xyz -coordinate system by a circular projected aperture of diameter $D = 60$ cm, a focal length $f = 39$ cm and a clearance $d' = 9$ cm, see Fig. 3. The feed is linearly polarized along x_f , where x_f, y_f, z_f is the feed coordinate system, with its origin at the focus and with z_f pointing towards the center point on the reflector.

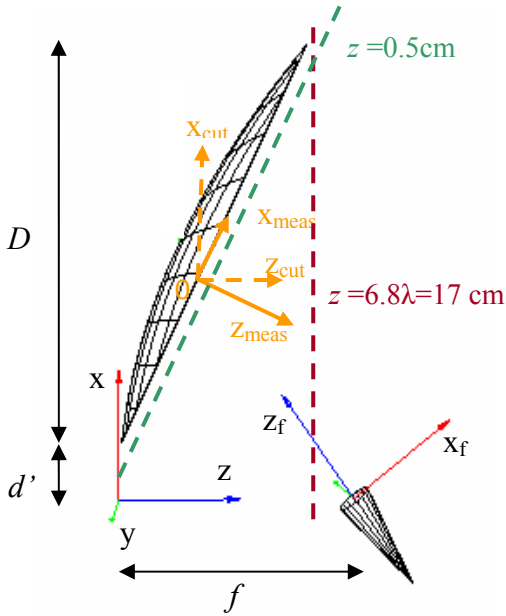


Figure 3. Offset reflector antenna: geometry and coordinate systems.

We introduce two coordinate systems (CS): the measurement CS, $x_{meas}, y_{meas}, z_{meas}$, with its origin on the reflector aperture plane and the z_{meas} -axis normal to that and coinciding with the horizontal rotation axis of the measurement system, and the cut CS, $x_{cut}, y_{cut}, z_{cut}$, obtained

by rotating $x_{meas}, y_{meas}, z_{meas}$ 26.5° around y_{meas} , and with z_{cut} thus aligned to the main beam direction. The measurement set-up of the antenna in its nominal configuration is shown in Fig. 4. By simply rotating the Q coefficients of the SWE of the radiated electric field measured in the measurement CS, the Q coefficients of the SWE in the cut CS are easily obtained [7]. The amplitude of the transformed far-field pattern, in the cut CS, of the antenna in its nominal configuration is plotted in dB in Fig. 5, showing co- and cross-polar components according to Ludwig's 3rd definition [7], in the uv -space, normalized to the maximum value of the co-polar component.

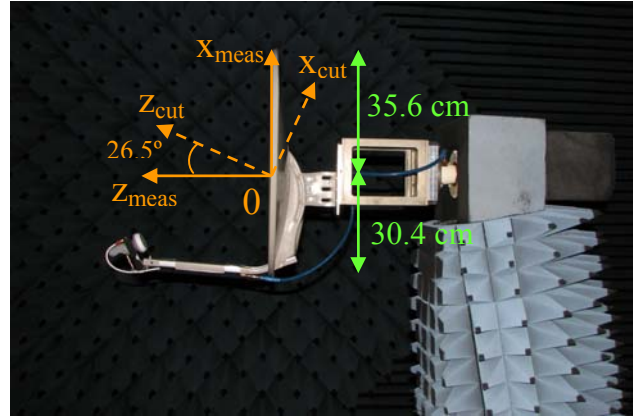


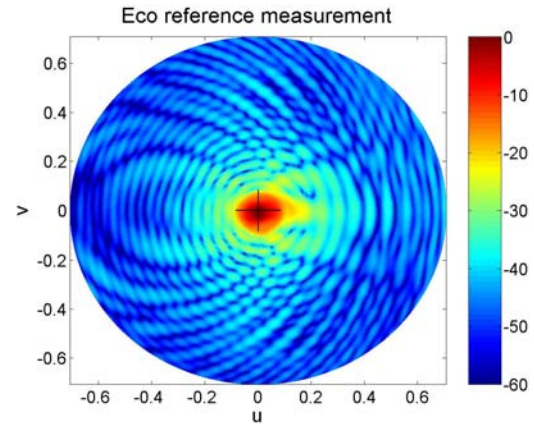
Figure 4. AUT on the measurement tower: geometry and coordinate systems.

From the Q coefficients the power spectrum

$$P_{rad}(n) = \frac{1}{2} \sum_{m=-n}^n |Q_{1mn}^{(3)}|^2 + |Q_{2mn}^{(3)}|^2$$

has been found, see Fig. 6.

It is seen that the finite dynamic range of the measurement system allows the correct acquisition of $N = 135$ modes which, with $r_o \approx 18\lambda$, corresponds to $N = kr_o + 22$, and $M = 120$.



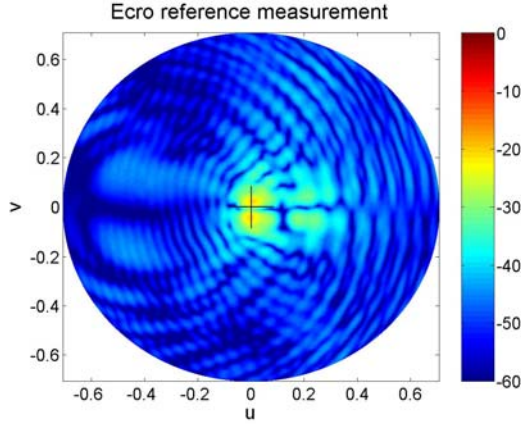


Figure 5. Amplitude of co- and cross-polar components in dB of the antenna far-field in its nominal configuration in the cut CS.

Truncating the mode spectrum at these two values, which will be used in all the subsequent investigated cases, retains more than 99.99% of the total radiated power.

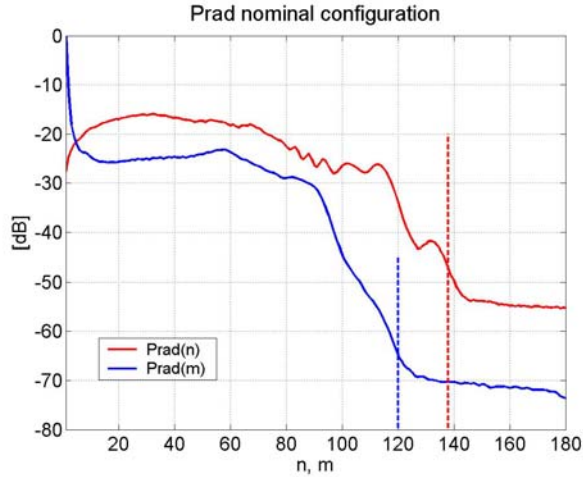


Figure 6. Power spectrum in the cut CS of the antenna in the nominal configuration and the truncation numbers $N=135$, $M=120$.

With these n - and m -truncations in the series of Eq. 3 it is expected to recover only the visible part of the plane wave spectrum and the singularity at $k_z = 0$. A calculation of the invisible region to improve the spatial resolution of the aperture fields is not possible here, since the number of available n -modes is not sufficient to reach convergence in the invisible region.

The Q coefficients of the SWE in the cut CS have thus been used to compute with Eq. 3 the plane wave spectrum $\bar{T}(k_x, k_y, z)$, in the $[-3k, 3k]$ spectral domain, on the z -plane $z = 17\text{cm} = 6.8 \lambda$, see Fig. 3. After replacing by zeros the values of the plane wave spectrum in the invisible region, the spectrum was inversely Fourier transformed obtaining the aperture field. Plots of the

amplitude of the x - and y -components of the electric field (in dB scale and normalized to the maximum of E_x), and phase of the x -component are shown in Fig. 7 on the z -plane $z = 17 \text{ cm}$ in the cut CS, where the projected circular rim of the reflector is also indicated. While the amplitude field distributions of E_x and E_y are almost symmetric around the $y=0$ axis, as expected, the phase distribution is not constant, as would be the case for an ideal parabolic reflector antenna, but shows a variation from the center of the aperture to the edge that reaches the maximum value of 2.4 rad. Thus, this reflector antenna – even in its nominal configuration – is far from ideal. By looking at the left side of the projected circular rim, we clearly distinguish the diffraction from the strut and the effect of the feed.

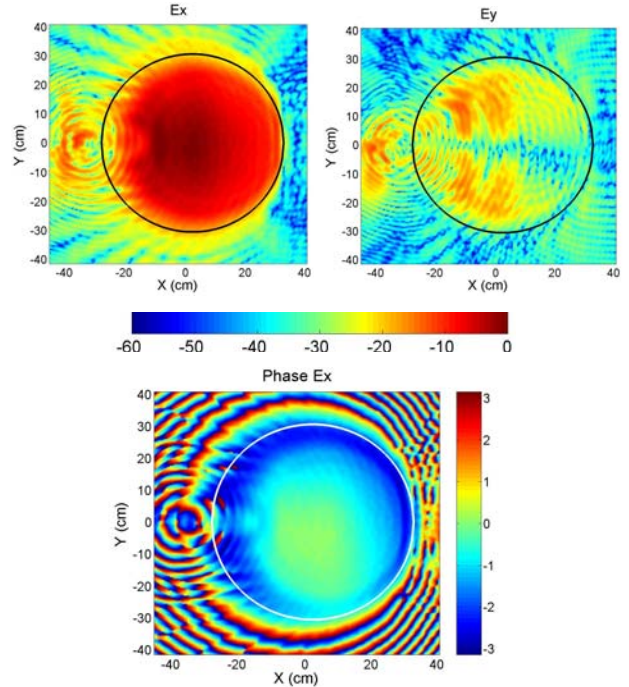


Figure 7. Amplitude of E_x and E_y and phase of E_x on $z=17 \text{ cm}$, in the cut CS for the nominal configuration.

4. Antenna errors: measurements and diagnostics results

4a) Feed tilt

Feed tilts of 5° and 10° around the x_f -axis have been considered, see Fig. 8. The tilt of the feed causes an asymmetry of the cross-polar far-field which is detectable already for the 5° case but becomes more evident for the 10° case, see Fig. 9. The Q coefficients of the SWE in the cut CS have been used to compute the plane wave spectrum $\bar{T}(k_x, k_y, z)$ on the z -plane $z = 17\text{cm}$.



Figure 8. Offset reflector with a feed tilt.

The amplitudes of the x - and y -components of the aperture field are shown in Fig. 10. When it is compared to Fig. 7, this clearly shows a tilt of the feed illumination towards the negative y -axis.

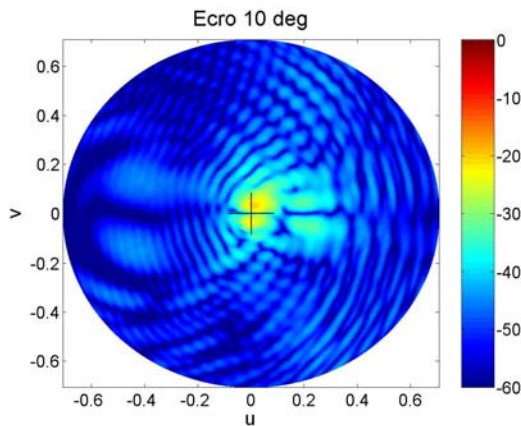


Figure 9. Amplitude of cross-polar component in dB of the antenna far-field for the 10° feed tilt case in the cut CS.

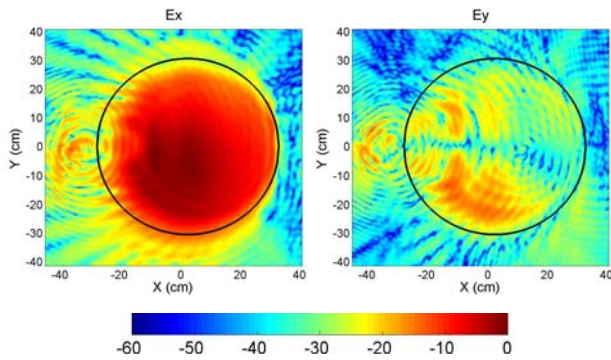


Figure 10. Amplitude of E_x and E_y on $z = 17$ cm, in the cut CS for the 10° feed tilt case.

4b) Gaussian bump

A metallic bump with the shape of a two-dimensional Gaussian function with peak and sigma both of 1 cm has been built and attached to the reflector surface, see Fig. 11. The co-polar component of the far-field pattern in the

cut CS is shown in Fig. 12. While the shape of the main beam is similar to the one of the nominal configuration in Fig. 5, the structure of the side-lobes changes significantly. The same was noticed for the cross-polar component. The aperture field was then calculated on the $z = 17$ cm plane in the cut CS, see Fig. 13 (left).

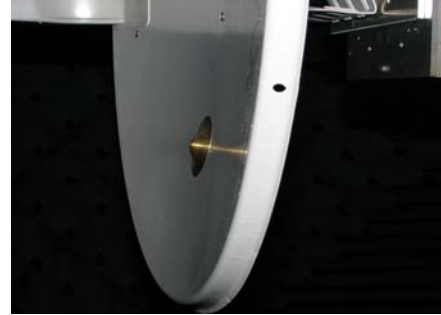


Figure 11. Offset reflector with a Gaussian bump.

On that plane also the z -component of the field (not shown here) highlights the circular structure caused by the bump.

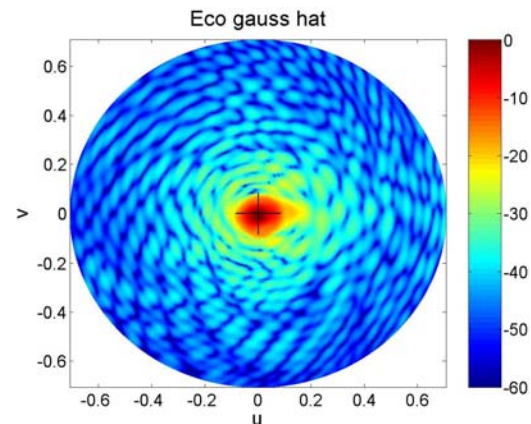


Figure 12. Amplitude of co-polar component of the antenna far-field for the Gaussian bump case in the cut CS.

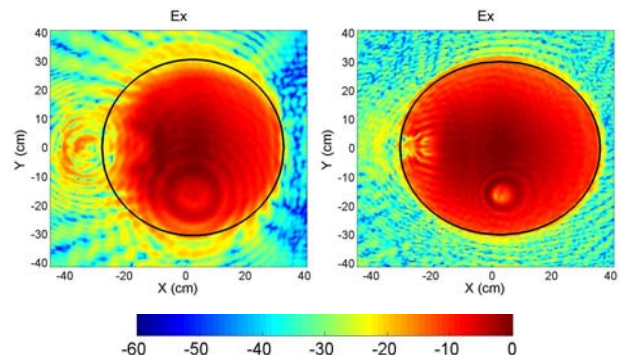


Figure 13. Amplitude of E_x on $z = 17$ cm in the cut CS (left), and on $z = 0.5$ cm in the measurement CS (right) for the Gaussian bump case.

Though the aperture illumination is now almost symmetric, when compared to Figs. 7 and 10, a circular structure of different amplitude is noticed for $x \approx 0$ cm and $y \approx -20$ cm. The picture becomes more clear when the aperture field is computed in the measurement CS on $z = 0.5$ cm, see Figs. 3 and 13 (right), where the projected elliptical rim of the reflector is also indicated.

4c) Surface distortion

A surface distortion was finally introduced by randomly placing 21 dishes of aluminum each with a diameter of 5 cm and thicknesses of 2.5 mm, 1.5 mm and 1 mm ($\lambda=2.5$ cm) on the entire reflector surface, see Fig. 14. This serves as a model of slowly varying surface distortions.



Figure 14. Offset reflector with surface distortions.

The co-polar component of the far-field is shown in Fig. 15. It is seen that side-lobes of high amplitude appear all around the main beam region, which remains almost the same as for the nominal configuration of Fig. 5.

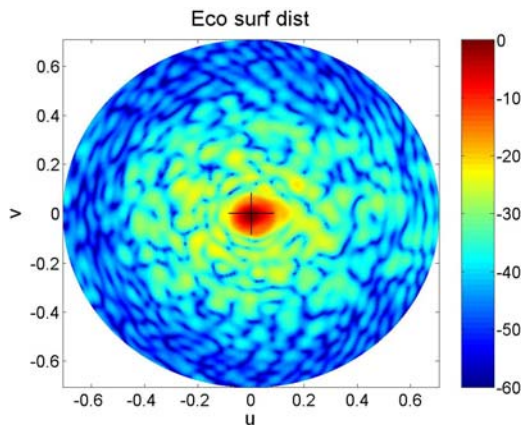


Figure 15. Amplitude of co-polar component of the antenna far-field for the surface distortion case in the cut CS.

The x -component of the aperture field is shown in Fig. 16, on the left at $z = 17$ cm in the cut CS, and on the right at $z = 0.5$ cm in the measurement CS. As for the Gaussian bump case, the distortions become more distinguishable on a plane closer to the reflector surface, in particular all

21 dishes, the thicker clearly, the thinner less strongly, are identified.

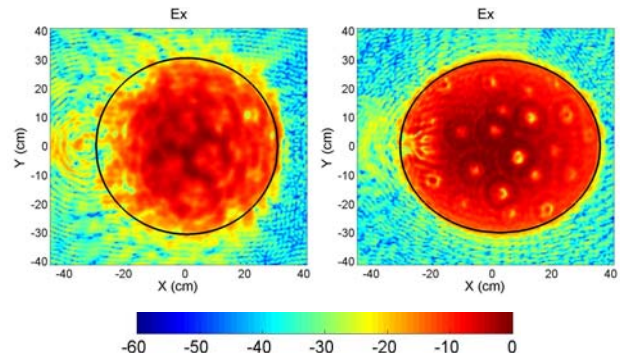


Figure 16. Amplitude of E_x on $z = 17$ cm in the cut CS (left), and on $z = 0.5$ cm in the measurement CS (right) for the surface distortion case.

5. Conclusions

A diagnostics of a simple commercially available offset reflector antenna for satellite TV reception has been performed by applying the SWE-to-PWE antenna diagnostics technique. The diagnostics showed that the antenna in its nominal configuration already exhibited non-ideal properties. Even in the presence of these, a feed tilt and two different types of surface distortions, which were intentionally introduced and provided anomalies in the far-field pattern, were correctly and accurately identified. The investigation serves as an experimental validation of the SWE-to-PWE antenna diagnostics technique in the presence of typical measurement inaccuracies and a non-ideal AUT. Furthermore, it highlights the value and importance of applying different coordinate systems and projected aperture planes for the purpose of antenna diagnostics.

REFERENCES

- [1] Kaplan L., Hanfling J. D., Borgiotti G. V., *The Backward Transform of the Near Field for Reconstruction of Aperture Field*, IEEE Ant. and Prop. Soc. Symp. Dig., 764 - 767, 1979.
- [2] Joy E. B., Guler M. G., *High Resolution Spherical Microwave Holography*, IEEE Trans. Ant. Prop., vol. 43, 464 - 472, 1995.
- [3] Rahmat-Samii Y., *Surface Diagnosis of Large Reflector Antennas Using Microwave Holographic Metrology: an Iterative Approach*, Radio Science., vol. 19, 1205-1217, 1984.
- [4] Homepage of the DTU-ESA Facility: http://www.oersted.dtu.dk/English/research/emi/afg/dtu_esa_facility.aspx.

[5] Cappellin C., Frandsen A., Breinbjerg O., *On the Relationship between the Spherical Wave Expansion and the Plane Wave Expansion*, AMTA Europe Symposium, Munich, Germany, 2006.

[6] Cappellin C., Breinbjerg O., Frandsen A., *The Influence of Finite Measurement Accuracy on the SWE-to-PWE Antenna Diagnostics Technique*, EuCap, European Conference on Antennas and Propagation, Nice, France, 2006.

[7] Hansen J. E., "Spherical Near-Field Antenna Measurements", Peter Peregrinus Ltd. London, 1988.

[8] Hansen T. B., Yaghjian A. D., "Plane Wave Theory of Time-Domain Fields, Near-Field Scanning Applications", IEEE PRESS, 1999.